A ternary Ni–Al–W EAM potential for Ni-based single crystal superalloys

Qin-Na Fan [a,b], Chong-Yu Wang [a,c,*], Tao Yu [a], Jun-Ping Du [a]

[a] Central Iron and Steel Research Institute, Beijing 100081, China
[b] College of Science, Northeastern University, Shenyang 110004, China
[c] Department of Physics, Tsinghua University, Beijing 100084, China

ARTICLE INFO

ABSTRACT

Based on experiments and first-principles calculations, a ternary Ni–Al–W embedded-atom-method (EAM) potential is constructed for the Ni-based single crystal superalloys. The potential predicts that W atoms do not tend to form clusters in γ(Ni), which is consistent with experiments. The impurity diffusion of W in γ(Ni) is investigated using the five-frequency model. The diffusion coefficients and the diffusion activation energy of W are in reasonable agreement with the data in literatures. By W doping, the lattice misfit between the two phases decreases and the elastic constants of γ'(Ni$_3$Al) increase. As for alloyed elements Co, Re and W, the pinning effect of solute atom on the γ(Ni)/γ'(Ni$_3$Al) misfit dislocation increases with the increasing of the atomic radius.

© 2014 Elsevier B.V. All rights reserved.

1. Introduction

Ni-based single crystal (SC) superalloys have been widely used in turbine blades of aero engines due to their superior high-temperature strength and creep resistance [1]. The excellent high temperature properties are inherited from the characteristic γ/γ' microstructure, with a large volume fraction of γ'(L1$_2$)-precipitates embedded in Ni-based γ(FCC)-matrix [2]. In order to improve the mechanical and chemical properties, more than ten alloying elements are added into superalloys [3] among which tungsten is considered as an important refractory element used to improve the creep resistance [4,5]. It was reported that W was particularly beneficial in improving the strength of the γ phase [1,6], reducing the coarsening rate of the γ' precipitates [7] and enhancing the hot corrosion resistance in Ni-based superalloys [5,8]. Besides, W can also considerably influence the lattice parameters of a_γ and $a_{\gamma'}$, as its larger atomic radius indirectly impacts the γ/γ' lattice misfit [9,10].

In the last decades, numerous research works related to the behavior of W in Ni-based SC superalloys had been completed using first-principles methods and experiments [4,11–13]. However, limited by the computer capacity, the first-principles simulation is incapable of the kinetic processes involving larger model size (more than 10,000 atom) and long simulation time ($\sim$1 ns). Compared with the first-principles simulation, molecular dynamics (MD) simulation, which has been widely used to study diffusion [14,15], dislocation motion [16–19] and crack propagation [20–22] in superalloys, is an efficient method to study the dynamic process at atomic level, and a promising method to explore the atomic mechanism of solute elements on the mechanical properties of superalloys.

An appropriate interatomic potential is crucial for MD simulations. Although the potentials [23–26] for Ni–Al binary system have been constructed, multi-element potentials containing alloying elements still need to be constructed for the applications in the γ(Ni)/γ'(Ni$_3$Al) superalloys. Yang et al. [27] employed the modified analytic embedded atom method (MAEAM) potential to study the alloying element (Re, Ru, Co, and Ta) dependence of the elastic properties of L1$_2$–Ni$_3$Al. In order to study the alloying effect of W in superalloys, a reliable Ni–Al–W potential is required. However, little research work was carried out to provide a Ni–Al–W ternary potential for the applications in superalloys.

Du et al. [28,29] had constructed a ternary Ni–Al–X (X denotes Re or Co) embedded-atom method (EAM) potential for the γ(Ni)/γ'(Ni$_3$Al) superalloys based on Cai–Ye [30] potential. By laying special emphasis on the effect of the embedding energy term of EAM, planar fault energies for Ni$_3$Al were improved. Based on this scheme, a ternary Ni–Al–W EAM potential is constructed and employed to study the alloying effect of W. The interaction between W and the γ(Ni)/γ'(Ni$_3$Al) interface is considered in the fitting of the present potential. The properties of W are studied

---

using the present potential. The impurity diffusion coefficient of W in γ(Ni) using the five-frequency model is calculated, subsequently the effective diffusion activation energy and the pre-exponential factor are obtained by fitting an Arrhenius equation to the diffusion coefficients. The effects of W on the lattice misfit and the elastic constants of γ'(Ni$_3$Al) are studied. The pinning effects of W and Co on the misfit dislocation are also investigated. It is demonstrated that the Ni–Al–W potential is suitable for MD simulations to understand the mechanical properties of the γ (Ni)/γ'(Ni$_3$Al) superalloys.

2. Construction of the potentials

2.1. Model of the potentials

In the scheme of EAM [31,32], the total energy of the system of N atoms is represented as:

$$E_{tot} = \sum_i F_i(\rho_i) + \sum_{i>j} \phi(r_{ij}), \tag{1}$$

where $F(\rho_i)$ is the embedding energy of atom i, and $\phi(r_{ij})$ is the pair potential between atoms i and j. The host electron density ρ_i is assumed to be the linear superposition of the atomic electron density $f(r_{ij})$, namely,

$$\rho_i = \sum_j f(r_{ij}). \tag{2}$$

The embedding energy function $F(\rho)$, atomic electron density $f(r_{ij})$ and pair potential $\phi(r_{ij})$ are taken the formulas used in our previous works [28,29]. Since the pair potentials for Ni–Ni, Al–Al and Ni–Al have been constructed, we just need to construct the potential for W and the pair potentials for Ni–W and Al–W.

The embedding energy function $F(\rho)$ [33] and the atom electron density $f(r)$ for W are taken the formulas as:

$$F(\rho) = -F_0 \left[1 - \ln\left(\frac{\rho}{\rho_e}\right)^n \right] \left(\frac{\rho}{\rho_e}\right)^n, \tag{3}$$

$$f(r) = s\tilde{f}(r)\psi\left(\frac{r-r_c}{h}\right), \tag{4}$$

$$\tilde{f}(r) = f_e \exp\left[-\chi(r-r_e)\right], \tag{5}$$

and

$$\psi(x) = \begin{cases} \frac{x^4}{1+x^4}, & x < 0 \\ 0, & x \geq 0 \end{cases}, \tag{6}$$

where $F_0 = E_c - E_v^f$, E_c and E_v^f are the cohesive energy and the vacancy formation energy, respectively. n is an adjustable parameter, and ρ_e represents the host electron density at equilibrium. s, r_c and h are adjustable parameters. f_e, χ and r_e are obtained by fitting the radial electron density calculated by Dmol3 [34,35]. $\Psi(x)$ is a cutoff function [36].

The pair potentials for W–W, Ni–W and Al–W are parameterized as:

$$\phi_{AB}(r) = \left\{ \phi_{Cai-Ye} - \gamma \exp\left[-\kappa(r/r_0 - 1)\right] + d_{AB}^A s_A \tilde{f}_A(r)/\rho_e^A \right.$$
$$\left. + d_{AB}^B s_B \tilde{f}_B(r)/\rho_e^B \right\} \psi\left(\frac{r-r_c}{h}\right), \tag{7}$$

where ϕ_{Cai-Ye} is the pair potential of Cai and Ye [30]. It is given by the equation:

$$\phi_{Cai-Ye} = -\alpha\left[1 + \beta(r/r_0 - 1)\right]\exp\left[-\beta(r/r_0 - 1)\right], \tag{8}$$

A=Ni, Al or W and B=W. r_0 in $\phi_{WW}(r)$ is the first-nearest neighbor of BCC–W. The parameter n in $F_W(\rho)$ and the parameters α, β, γ, κ, d_{WW}^W, h, r_c in $\phi_{WW}(r)$ are determined by fitting the

properties of BCC–W. The parameter s_W in $f(r)$ and parameters α, β, γ, κ, r_0, d_{AB}^A, d_{AB}^B, h, r_c in $\phi_{NiW}(r)$ and $\phi_{AlW}(r)$ are given by fitting the first-principles data of virtual compounds.
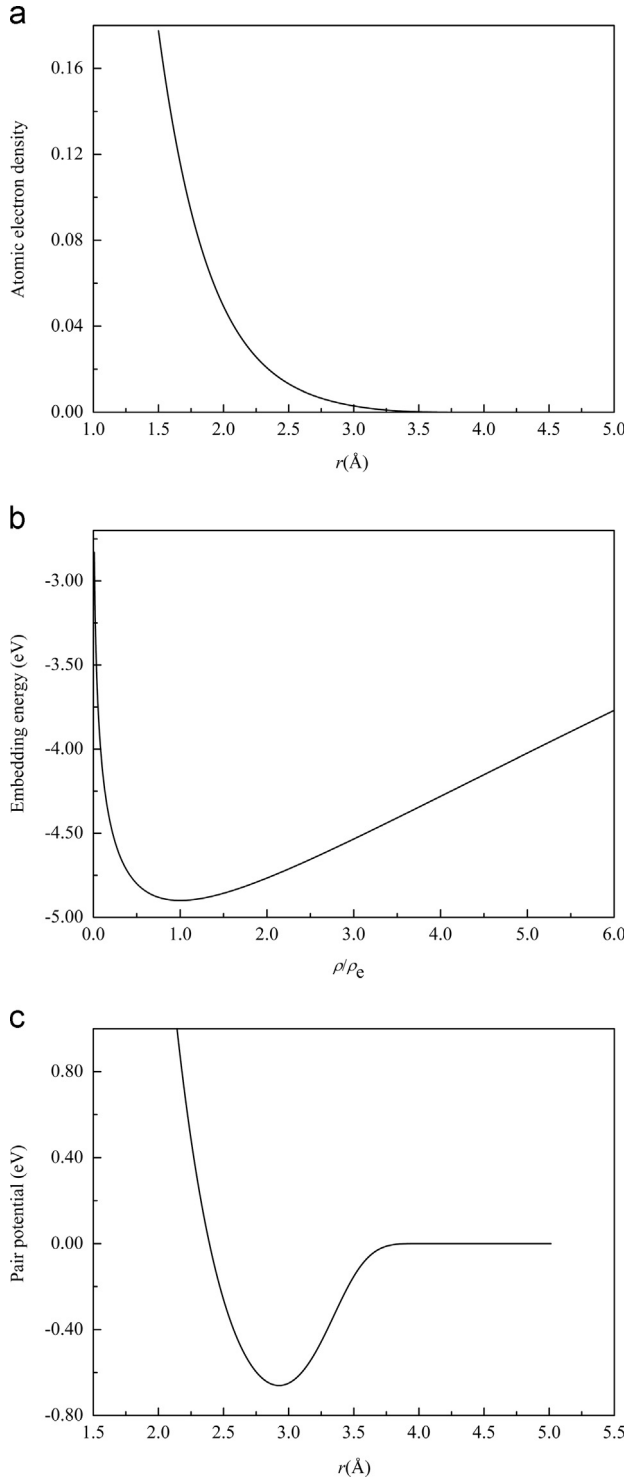
2.2. Fitting the potentials

The properties used in the fitting of potential for BCC–W include the lattice parameter a, cohesive energy E_c, elastic constants C_{ij}, vacancy formation energy E_v^f and Rose equation [37]. The parameters in the potential are given by minimizing the weighted mean square deviation between the calculated and experimental data. The optimized parameters are listed in Table 1. The atomic electron density, embedding energy and pair potential for W are plotted in Fig. 1(a)–(c) respectively. The properties calculated with the different potentials are listed in Table 2, in comparison with those from experiments or first-principles calculations. The lattice parameter a, cohesive energy E_c, elastic constants C_{ij}, vacancy formation energy E_v^f and vacancy migration E_v^m calculated with the present and other potentials are in excellent (less than 1% deviation) agreement with the experimental data. The surface energies of three low-index faces {1 0 0} {1 1 0} and {1 1 1} are also calculated with the present potential. It can be found from Table 2 that the present, Johnson [46], FS [47] and MAEAM [41] potentials yield similar values for the surface energies, and they remarkably underestimate the experimental data [48,49] (more than 200 mJ/m^2). On the contrary, the MEAM potential [40] predicts larger surface energies. Furthermore, the order calculated with the present potential for the three surface energies is $E\{1\,1\,0\}$ $\langle E\{1\,0\,0\}\langle E\{1\,1\,1\}$, which is in agreement of experimental information [51]. In addition, all potentials predict the {1 1 0} surface to be more stable than the {1 0 0} surface. We also calculated two important points on the generalized stacking fault energy profile (γ-surface) of the $(\bar{1}\,1\,0)$ plane along the [1 1 1] direction, namely γ $(\bar{1}\,1\,0)$ ($\mathbf{b}/3$) and γ $(\bar{1}\,1\,0)$ ($\mathbf{b}/6$), where $\mathbf{b} = 1/2\langle 1\,1\,1\rangle$. The deviations of the calculation results of γ $(\bar{1}\,1\,0)$ ($\mathbf{b}/3$) and γ $(\bar{1}\,1\,0)$ ($\mathbf{b}/6$) between the present potential and the first-principles are less than 10%.

The equation of state for W is plotted in Fig. 2. It is seen from Fig. 2 that the equation of state using the present potential is in reasonable agreement with the Rose equation. For a metal with structure A, the energy of structure stability is defined as $\Delta E = E_B - E_A$, E_A and E_B are the cohesive energies with A and B structures, respectively. The energies of structure stability for BCC–W with respect to FCC, HCP, SC and diamond structures are listed in Table 3. It can see from Table 3 that the order of stability energies calculated with the present potential is consistent with that calculated using the Vienna ab initio simulation package (VASP) [52,53].

The parameters of Ni–W and Al–W pair potentials are obtained by fitting the first-principles calculation data of different virtual structure compounds. These calculation data include the lattice constants and the binding energies. The virtual structures are as follows: L1$_2$–Ni$_3$W, D0$_{19}$–Ni$_3$W, D0$_{22}$–Ni$_3$W, B2–NiW, L1$_2$–W$_3$Al,

Table 1
Potential parameters of the present EAM potential for W.

Parameter	Value	Parameter	Value
κ	1.3308	h (1/Å)	0.7820
α (eV)	1.1531	r_c (Å)	4.0134
β	1.6850	r_0 (Å)	2.7366
d_{WW}^W (eV)	1.8541	f_e	4.02×10^{-3}
n	3.1310×10^{-1}	r_e (Å)	2.75
γ (eV)	-3.2338×10^{-2}	χ (1/Å)	2.5401
ρ_e	3.4157×10^{-2}		

Fig. 1. (a) Atomic electron density, (b) embedding energy and (c) pair potential for W.

B2–WAl, L1$_2$–Al$_3$W and L2$_1$–Ni$_2$WAl. The first-principles calculations are performed by using the VASP. The property of site preference is also considered in the fitting. Binding energies of two models Ni$_{24}$Al$_7$W and Ni$_{23}$Al$_8$W are included in the fitting data. Ni$_{24}$Al$_7$W model is a $2 \times 2 \times 2$ Ni$_3$Al supercell with an Al atom replaced by W and Ni$_{23}$Al$_8$W model is a $2 \times 2 \times 2$ Ni$_3$Al supercell with a Ni atom replaced by W. According to Jiang [54], $E_W^{Ni \to Al}$ describes the site preference behavior of a ternary element in the

γ'(Ni$_3$Al), and its expression is

$$E_W^{Ni \to Al} = E(Ni_{24}Al_7W) - E(Ni_{23}Al_8W) + E(Ni_{23}Al_8Al) - E(Ni_{24}Al_8),$$
(9)

where E(Ni$_{23}$Al$_8$Al) is the binding energy of a $2 \times 2 \times 2$ Ni$_3$Al supercell with one Ni replaced by Al. Eq. (9) characterizes the energy required in transferring a W atom from a Ni sublattice to an Al sublattice. $E_W^{Ni \to Al}$ calculated using the present potential is -0.14 eV/atom. It means that W prefers to occupy the Al sublattice, which is consistent with the experimental result [55].

In order to enlarge the applicability of the present potential, the interaction between W and the γ(Ni)/γ'(Ni$_3$Al) interface is particularly considered in the fitting. Four W-addition γ(Ni)/γ'(Ni$_3$Al) interface supercell models, named Ni(1), Ni(2), Ni(3) and Al(4), are constructed by replacing the labeled atoms with W (see Fig. 3). The γ(Ni)/γ'(Ni$_3$Al) interface supercell model contains 64 atom and two interfaces. In Fig. 3, the atoms replaced by W in the Ni(1), Ni(2), Ni(3) and Al(4) models are labeled with '1', '2', '3' and '4', respectively. The pure Ni/Ni$_3$Al model is referred to as Noadd. The heats of formation of the four W-addition Ni/Ni$_3$Al interface supercell models are used in the fitting. The following expression is adopted to calculate the heat of formation per atom of a supercell [56]:

$$H = [E_i(n, m, l) - n \times E_b(Ni) - m \times E_b(Al) - l \times E_b(W)]/(n + m + l),$$
(10)

where $E_i(n, m, l)$ is the binding energy of the supercell with n, m and l atoms of Ni, Al and W. $E_b(Ni)$, $E_b(Al)$ and $E_b(W)$ are the binding energies per atom for the monoatomic metals of Ni, Al and W, respectively.

The pair potential parameters for Ni–W, Al–W and the parameter s_W are given by minimizing the weighted mean square deviation between the calculated and the first-principles data. In order to match the experiment values, the binding energies $E_i(n, m, l)$ are scaled by the equation:

$$H^{FP} = [E_i(n, m, l) - n \times E_b^{EXP}(Ni) - m \times E_b^{EXP}(Al) - l \times E_b^{EXP}(W)]/(n + m + l),$$
(11)

where H^{FP} is the heat of formation per atom calculated with the first-principles using Eq. (10). $E_b^{EXP}(Ni)$, $E_b^{EXP}(Al)$ and $E_b^{EXP}(W)$ are the experimental binding energies per atom. The optimized parameters are listed in Table 4. The lattice parameters and binding energies of the virtual compounds used in the fitting and the calculated values with the present EAM potential are listed in Table 5. The lattice constants and the binding energies of the ordered structures are in good agreement with the VASP calculations, with a root-mean-square deviation of 2.3%. Pair potentials for Ni–W and Al–W are plotted in Fig. 4. The lattice parameters and binding energies of the virtual Ni–W structure compounds fit better than those of Al–W structures. The heats of formation of the pure and the four W-addition γ(Ni)/γ'(Ni$_3$Al) interface supercell models calculated with the present potential and VASP are listed in Table 6. The order of the heats of formation calculated using the present potential is as follows, Ni(1) < Ni(2) < Noadd < Al(4) < Ni(3), which is consistent with the order calculated with VASP.

The behavior of W atoms in γ(Ni) is investigated using the present potential. The binding energy of n W atoms is evaluated using a $3 \times 3 \times 3$ supercell (108 atom) and is given by the following equation:
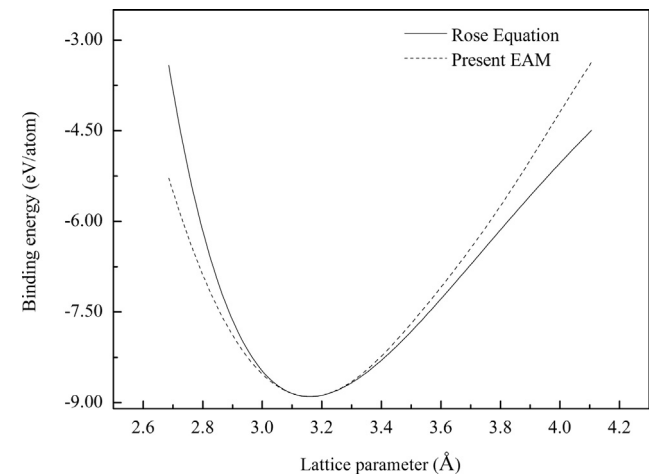
$$E_{binding}(nW) = E(Ni_{108-n}W_n) + (n-1) \times E(Ni_{108}) - n \times E(Ni_{107}W_1),$$
(12)

where E(Ni$_{108}$), E(Ni$_{107}$W$_1$) and E(Ni$_{108-n}$W$_n$) are the energies of the pure Ni lattice, the Ni lattice containing one W atom and the Ni lattice with n W atoms placed at the first or second nearest neighboring (1NN or 2NN) sites (see Fig. 5), respectively. A positive

Table 2
Properties of W calculated with the present potential and other potentials, compared with experimental or first-principles data.

	Experiment or first-principles	Johnson	F–S	MEAM [40]	MAEAM [41]	Present potential
a_0 (Å)	3.16 [42][a]	3.16[38]	3.17[39]	3.16	3.17	3.16
E_C (eV)	8.90 [1][a]	8.66[38]	8.90[39]	8.66	8.90	8.90
Elastic constants (GPa)						
C_{11}	523.0 [43][a]		522.4[39]	532.6	517	522.9
C_{12}	203.0 [43][a]		204.4[39]	205.0	203	203.0
C_{44}	160.0 [43][a]		160.6[39]	163.1	157	160.0
Vacancy formation and migration energies (eV)						
E_v^f	4.0 ± 0.3 [44] [a]	3.95[38]	3.71[41]	3.95	3.95	4.02
E_v^m	2.0 [45]	1.97[46]	1.49[47]	1.61	1.55	1.98
Surface energies (mJ/m^2)						
{1 0 0}		2809[46]	2924[47]	3900	2858	2858
{1 1 0}		2599[46]	2575[47]	3427	2614	2627
{1 1 1}				4341		3209
Average	3250 [48], 3675 [49]					
Generalized stacking fault energy (meV/Å^2)						
$\gamma(\bar{1}\,1\,0)(\boldsymbol{b}/3)^b$	112.64 [50]					101.00
$\gamma(\bar{1}\,1\,0)(\boldsymbol{b}/6)^b$	42.67 [50]					39.34

[a] Included in the fitting.
[b] Calculated by VASP.

Fig. 2. Equations of state for W using the present EAM potential and the Rose equation.

Fig. 3. Atomic configurations of the pure and W-addition γ(Ni)/γ'(Ni$_3$Al) interfacial models. The blue and pink balls denote Ni and Al atoms, respectively. The pure Ni/Ni$_3$Al model is referred to as Noadd. The atoms labeled with 1, 2, 3 and 4 are replaced by W in the Ni(1), Ni(2),Ni(3) and Al(4) models, respectively.
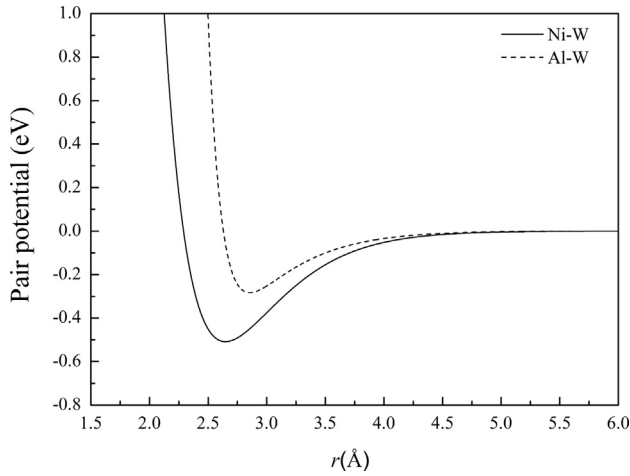
Table 3
Energies (eV/atom) of structure stability for BCC–W.

Structure	VASP	Present model
FCC	0.49	0.07
HCP	0.45	0.06
SC	1.43	2.18
Diamond	2.63	2.95

Table 4
Optimized parameters of the pair potentials for Ni–W, Al–W and s_W.

W–Ni		W–Al	
Parameter	Value	Parameter	Value
α (eV)	6.8329	α (eV)	−2.9222
β	5.8701	β	7.4099
γ (eV)	16.542	γ (eV)	−134.80
κ	6.7310	κ	16.459
r_0 (Å)	2.0741	r_0 (Å)	1.9828
d_{NiW}^{Ni} (eV)	20.4842	d_{AlW}^{Al} (eV)	−11.9952
d_{NiW}^{W} (eV)	29.794	d_{AlW}^{W} (eV)	1.42982
h (Å^{-1})	0.2298	h (Å^{-1})	0.4472
r_c (Å)	6.1460	r_c (Å)	5.5951
s_W	1.9472		

binding energy indicates a repulsive force between n W atoms while a negative one indicates an attractive force. It can be seen from Fig. 5(a) and (b) that the binding energies of 1NN and 2NN clusters calculated with the present potential increase with the increasing of the number of W atoms. Both the binding energies of 1NN and 2NN clusters are energetically unfavorable in Ni, which indicates that the W atoms do not tend to form clusters in γ(Ni). This result is consistent with the experiments [57–59].

Table 5
Properties used in the fitting of the cross interactions of Ni–W and Al–W obtained from VASP calculations and compared with the present potential.

Formula	Structure	Lattice constants(Å)		Binding energy (eV/atom)	
		First-principles	EAM	First-principles	EAM
Ni$_3$W	L1$_2$	3.64	3.61	−5.44	−5.73
Ni$_3$W	D0$_{19}$	$a=5.09$	5.10	−5.60	−5.71
		$c/a=0.84$	0.82		
Ni$_3$W	D0$_{22}$	$a=3.58$	3.57	−5.64	−5.75
		$c/a=2.07$	2.07		
NiW	B2	3.00	2.99	−6.33	−7.08
Al$_3$W	L1$_2$	3.94	4.02	−4.68	−4.45
WAl	B2	3.13	3.20	−5.79	−5.72
W$_3$Al	L1$_2$	3.98	4.07	−7.30	−7.18
Ni$_2$WAl	L2$_1$	5.91	5.83	−5.44	−5.57
Ni$_{24}$Al$_7$W	Supercell $2 \times 2 \times 2$	3.58	3.58	−4.77	−4.79
Ni$_{23}$Al$_8$W	Supercell $2 \times 2 \times 2$			−4.74	−4.75

Fig. 4. Pair potentials for Ni–W and Al–W.

Table 6
Heats of formation of pure and W-addition γ(Ni)/γ'(Ni$_3$Al) interface models calculated with the present potential and from VASP.

| Model	The heat of formation (eV/atom)	
	VASP	Present work
Ni(1)[a,b]	−0.27	−0.28
Ni(2)[a,b]	−0.25	−0.25
Ni(3)[a,b]	−0.20	−0.20
Al(4)[a,b]	−0.22	−0.21
Noadd[b]	−0.24	−0.24

[a] Included in the fitting database.
[b] Relaxed with respect with unit cell volume, shape and all internal position.

3. Applications and discussion

3.1. Impurity diffusion of W in γ(Ni)

The diffusion of alloying elements is of great importance on the mechanical performance in Ni-based SC superalloys. The kinetics of microstructural changes and the processes of mass transport are governed by the rate of atomic diffusion at the elevated temperatures [60,61]. The diffusion of alloying elements is correlated with the creep deformation [62] and the directional coarsening of the γ' phase [63] in Ni-based superalloys. Furthermore, oxidation occurs at a rate associated with diffusion-controlled [64]. To investigate
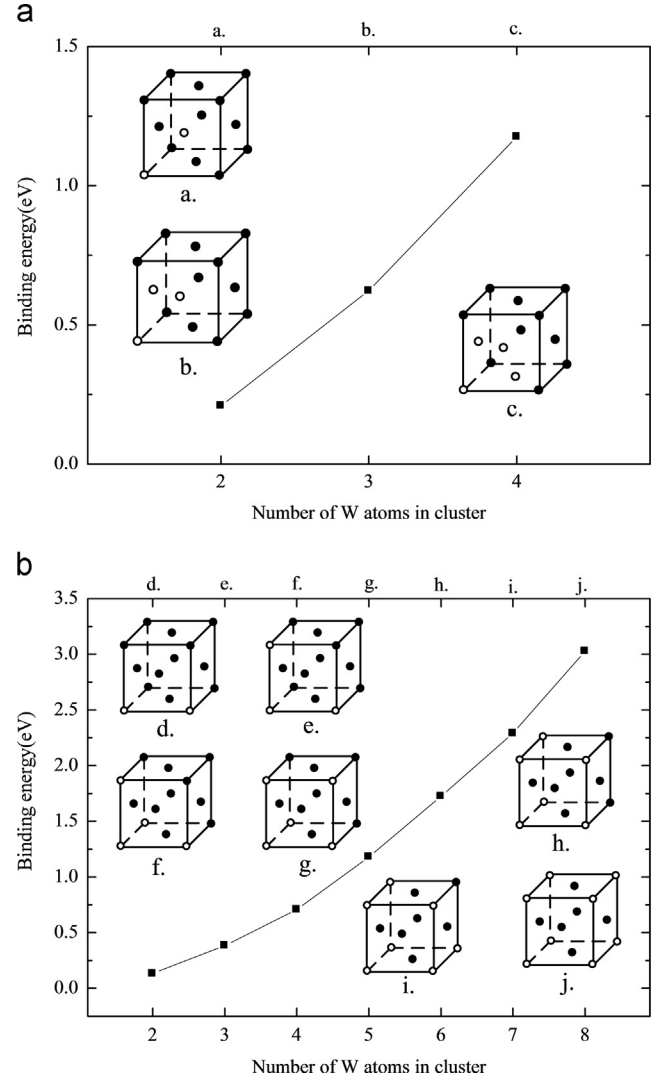
Fig. 5. Binding energies of (a) 1NN and (b) 2NN W clusters in a $3 \times 3 \times 3$ FCC–Ni supercell. The atomic configurations of W clusters (a.)–(j.) are shown in the insets. The black and white balls denote Ni and W atoms, respectively.

the diffusion behaviors of W in superalloys using MD simulation, it is crucial whether the diffusion activation energy is accurate.

The diffusion activation energy Q for W atom at 0 K is calculated by the following equations:

$$Q = E_f^V + E_b, \tag{13.a}$$

$$E_f^V = E_f^{W-V} + E_f^{V(Ni)}, \tag{13.b}$$

$$E_f^{W-V} = E(\text{Ni}_{N-2}\text{WV}) - E(\text{Ni}_{N-1}\text{W}) - E(\text{Ni}_{N-1}\text{V}) + E(\text{Ni}_N), \tag{13.c}$$

where E_f^V is the vacancy formation energy for an atom adjacent to a W atom. E_b is the diffusion barrier of W in Ni. E_f^{W-V} and $E_f^{V(Ni)}$ denote the W-vacancy binding energy and the vacancy formation energy in Ni, respectively. $E(\text{Ni}_{N-2}\text{WV})$ represents the energy of a N-atom system with a W-vacancy pair. $E(\text{Ni}_{N-1}\text{W})$ and $E(\text{Ni}_{N-1}\text{V})$ represent the energies of two N-atom systems including a W atom and a vacancy, respectively. E_f^V and E_b calculated with the present potential are 1.80 eV and 1.25 eV, respectively. Therefore, the diffusion activation energy is 3.05 eV. It reproduces the first-principles calculation results 3.05 eV [60,61] and 2.98 eV [65] successfully.

It is accepted that impurity elements diffuse in FCC crystals via the vacancy mechanism [66]. This vacancy mechanism is well described by the five-frequency model [67]. The ratio of impurity diffusion rate D_s to self-diffusion rate D_0 is

$$\frac{D_s}{D_0} = \frac{f_2}{f_0} \frac{w_2}{w_1} \frac{w_4}{w_0} \frac{w_1}{w_3}, \qquad (14)$$

where f_2 is the impurity correlation factor. f_0 is the self-diffusion factor. w_0 is the vacancy jump frequency in the crystal. $w_i (i=1-4)$ are the jump frequencies in Fig. 6. w_{3a}, w_{3b} and w_{3c} are the vacancy jump frequencies from the site adjacent to the impurity to the 2nd, 3rd and 4th nearest neighbor sites, respectively. $w_{4(a,b,c)}$ are the reverse jump frequencies of $w_{3(a,b,c)}$. The activation barrier energies of the three w_3 are found to be identical within 0.02 eV. Since the fourth nearest neighbor positions are most similar to the bulk positions, the values of w_{3c} and w_{4c} are used. For FCC crystal, $f_0 = 0.715$. f_2 which is a function of the jump frequencies and the diffusion activation barrier energies can be calculated [4,65,68]. Provided the self-diffusion rate and the diffusion activation barrier energies are known, the diffusion rate of impurity can be obtained using the approximations reported in [69]. The self-diffusion data of Ni [70] are used to calculate the impurity diffusion coefficient. Note that the activation energy of w_2 is the $E_b = 1.25$ eV. The activation energies of w_1, w_{3c} and w_{4c} calculated with the present model are 1.23, 0.89 and 1.14 eV, respectively.

The calculated diffusion coefficients of W in this study and the experimental data [71–73] are shown in Fig. 7. It can be seen in Fig. 7 that the diffusion coefficients calculated using the five-
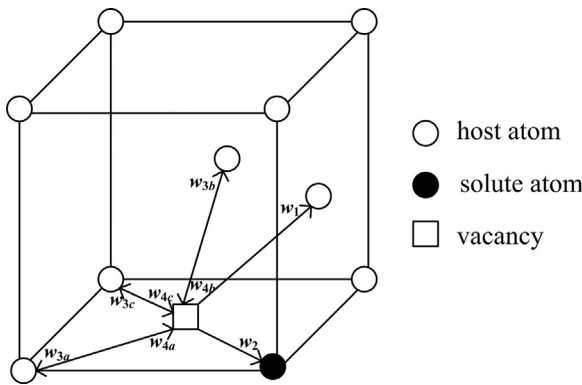

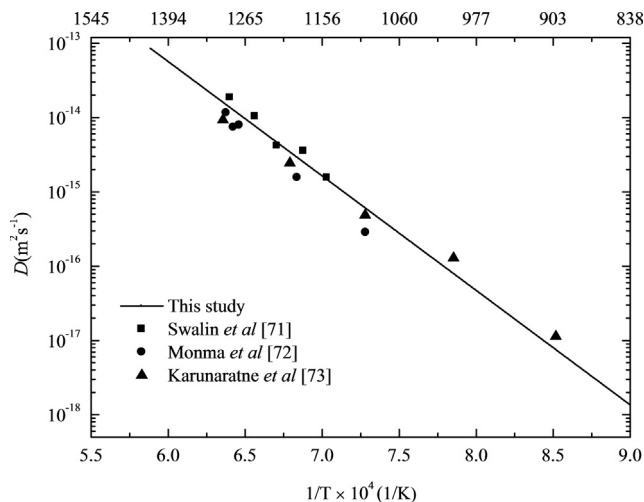**Fig. 6.** Vacancy jumps in FCC crystal near an impurity.

Fig. 7. Calculated diffusion coefficients of W and compared with experimental data.

Table 7
Calculated values of Q_e and D_0 by fitting the obtained diffusion coefficients and the corresponding cited values.

	$D_0 (m^2/s)$	$Q_e (eV)$	$Q_e (kJ/mol)$	Temperature range (°C)
Calculated				
Present Model	9.78×10^{-6}	3.05	294.14	
Campbell et al. [74]	2.79×10^{-5}	2.93	282.13	
Karunatatne et al. [75]	3.90×10^{-4}	3.24	312.43	
Wu et al. [65]	2.10×10^{-4}	3.14	302.51	
Experiment				
Swalin et al. [71]	1.11×10^{-6}	3.33	321.55	1153–1289
Monma et al. [72]	1.9×10^{-7}	3.10	299.36	1100–1295
Karunatatne et al. [73]	8.0×10^{-6}	2.74	264.0	900–1300

frequency model are basically consistent with the experimental data [71–73] at high temperatures (above 1000 °C). While the experimental data available for the diffusion at lower temperatures (below 1000 °C) is limited, the diffusion coefficients underestimate the experimental data [73]. The diffusion coefficient as a function of temperature follows the Arrhenius law $D = D_0 \exp(-Q_e/kT)$. The effective diffusion activation energy Q_e and pre-exponential factor D_0 are determined by fitting the obtained diffusion coefficients. The obtained values of Q_e and D_0 compared with corresponding calculated [65,74,75] and experimental [71–73] values are listed in Table 7. It can be seen from Table 7 that Q_e reproduces the EAM value of Q.

Compared with the other calculated models [65,74,75], the obtained value of D_0 calculated using the present model is most close to experimental values. All the calculated values of Q_e fall in the range of experimental values. The value of Q_e determined by fitting the experimentally measured diffusion coefficients [73] is slight less than those in other models. One possible reason for this discrepancy could be the different diffusion mechanisms at high and low temperatures. Vacancy exchange diffusion is assumed as the mediate mechanism at higher temperatures. However, fast grain boundary diffusion which might be expected to make certain contribution to the diffusion processes at lower temperatures (see Fig. 7), which results in low values of Q_e.

3.2. Effects of W on the lattice misfit and elastic constants of $\gamma'(Ni_3Al)$

The γ/γ' lattice misfit and the elastic constants are correlated with the mechanical properties of superalloys [76,77]. A smaller γ/γ' lattice misfit can minimize the γ/γ' interfacial energy so that the γ' directional coarsening, known as rafting, is restricted [78,79]. The lattice misfit is:

$$\delta = 2\frac{a_{\gamma'} - a_\gamma}{a_{\gamma'} + a_\gamma}, \qquad (15)$$

where a_γ and $a_{\gamma'}$ are the lattice parameters of the γ and γ' phases, respectively. In order to investigate the influence of W on the interface lattice misfit, four simulation boxes including $\gamma(Ni)$, γ' (Ni_3Al), alloyed $\gamma(Ni(W))$ and $\gamma'(Ni_3(Al,W))$ were constructed. Each box consisted of 4000 atom. The magnitude of $\gamma(Ni)$ and $\gamma'(Ni_3Al)$ were $10a_\gamma \times 10a_\gamma \times 10a_\gamma$, and $10a_{\gamma'} \times 10a_{\gamma'} \times 10a_{\gamma'}$, respectively. The X, Y and Z axes of the box were along the [1 0 0], [0 1 0] and [0 0 1] directions, respectively. Alloyed $\gamma(Ni(W))$ was constructed as follows: firstly, a $2 \times 2 \times 2$ FCC–Ni supercell with a Ni atom replaced by a W atom was constructed and then the supercell was enlarged to a simulation box of $10a_\gamma \times 10a_\gamma \times 10a_\gamma$. Similarly, a $2 \times 2 \times 2$ L1$_2$–Ni$_3$Al supercell with an Al atom replaced by a W atom was constructed and then enlarged to a simulation box of $10a_{\gamma'} \times 10a_{\gamma'} \times 10a_{\gamma'}$ as alloyed $\gamma'(Ni_3(Al,W))$.

The lattice parameters of the models at 0 K were obtained by minimizing the total energies of the supercells with respect to the

local atomic displacements and the supercell volume. The lattice parameters at 293 K were obtained by relaxing the simulation boxes in NPT ensemble. In all MD simulations, the time step was 2×10^{-15} s and periodic boundary conditions were used. The simulation results demonstrate that the lattice parameters and lattice misfits calculated using the present potential are in agreement with those calculated using VASP [80], as shown in Table 8. The lattice parameters of γ(Ni) and γ'(Ni$_3$Al) at 293 K are 3.531 Å and 3.580 Å, respectively, which are slightly larger than the experimental data of 3.52 Å [40] and 3.567 Å [81]. Due to the larger atomic radius of the element W, the addition of W results in the increasing of lattice parameter. The lattice parameter increment of γ(Ni) is larger than that of γ'(Ni$_3$Al), which leads to the decreasing lattice misfit.

The alloying effect of W on the elastic constants C_{ij} of γ'(Ni$_3$Al) at both 0 K and 293 K were investigated. The elastic constants of the supercells at 0 K were obtained by deforming the supercells and measuring the change in the stress tensor. The elastic constants at 293 K were obtained by measuring the change in average stress tensor in an NVT (canonical) simulation when the cell volume undergone a small deformation at the equilibrate system. The calculated results are shown in Table 9. The calculated C_{ij} of γ'(Ni$_3$Al) at 293 K are in reasonable agreement with the experimental data [82–84]. The calculated elastic constants C_{ij} of γ'(Ni$_3$Al) at 293 K using the present potential are smaller than those at 0 K, which is in accordance with the trend of experimental results [82–84]. The elastic constants increase due to the addition of W at both 0 K and 293 K, which is in agreement with the first-principles calculations. This means that the present potential is suitable to describe the material constants of the W doped γ'(Ni$_3$Al).

3.3. Interaction between W and the misfit dislocation on the γ(Ni)/γ'(Ni$_3$Al) interface

It is demonstrated that the γ/γ' interfacial dislocation networks have a close relationship with the creep strength as they protect

Table 8
Calculated lattice parameters and lattice misfits of γ(Ni), γ'(Ni$_3$Al), alloyed γ(Ni(W)) and γ'(Ni$_3$(Al,W)) with the present potential and from first-principles calculations.

|	VASP[80]		Present EAM (0 K)		Present EAM (293 K)	
	a (Å)	δ (%)	a (Å)	δ (%)	a (Å)	δ (%)
γ(Ni)	3.515	1.50	3.520	1.33	3.531	1.38
γ'(Ni$_3$Al)	3.568		3.567		3.580	
γ(Ni (W))	3.536	1.10	3.539	1.07	3.547	1.18
γ'(Ni$_3$(Al,W))	3.576		3.577		3.589	

Table 9
Calculated elastic constants (GPa) of γ'(Ni$_3$Al) and alloyed γ'(Ni$_3$(Al,W)) with the present potential in comparison with the first-principles calculation and the experiments.

	C_{11}	C_{12}	C_{44}
Ni$_3$Al			
VASP [80]	229.7	147.5	116.6
Present EAM (0 K)	242.6	149.3	130.3
Present EAM (293 K)	230.0	147.5	125.1
Exp. 1 (283 K) [82]	220.6	146.1	124.0
Exp. 2 (293 K) [83]	223.4	148.2	125.2
Exp.3 (296 K) [84]	198.0	126.6	117.9
Ni$_3$(Al,W)			
VASP [80]	248.1	152.5	121.5
Present EAM (0 K)	246.4	153.2	132.6
Present EAM (293 K)	238.4	150.0	125.5

the γ' precipitates from shearing by the γ matrix dislocations [85–89]. The formation of the misfit dislocation networks at the γ/γ' interfaces relieves the coherency stress. Moreover, the γ/γ' interfacial dislocation networks play an important role in the directional coarsening of the γ' phase by inducing the local chemical concentration gradients in different γ matrix corridors [90–93].The pinning effect of the alloying elements on the misfit dislocation makes the γ/γ' interface more stable. In order to study the pinning effect of W on the misfit dislocation, the interaction energy between W and the misfit dislocation was calculated by employing a single impurity model. The interaction between a single solute atom and the misfit dislocation is local, thus the Al atom in the γ (Ni) within the localized region could be neglected. Therefore, FCC–Ni and L1$_2$–Ni$_3$Al were taken as γ(Ni) and γ'(Ni$_3$Al), respectively. The γ(Ni)/γ'(Ni$_3$Al) interface model with the (0 0 1) interface oriented along the axes X=[1 1 0], Y=[$\bar{1}$ 1 0], and Z=[0 0 1] was constructed, as shown in Fig. 8. The model included two parts, the upper part was γ'(Ni$_3$Al) with box vectors 37 [1 1 0], 37 [$\bar{1}$ 1 0], and 15 [0 0 1]; The lower part was γ(Ni) with box vectors 37.5 [1 1 0], 37.5[1 1 0], and 15 [0 0 1]. The lattice parameters of γ(Ni) and γ'(Ni$_3$Al) were 3.52 Å and 3.567 Å, respectively. The box vectors were selected to make sure the Burgers vector of the dislocations be 1/2⟨1 1 0⟩ type, which was consistent with the experimental observation [90,94]. The model was periodic along the X and Y directions and had free surfaces on the upper and lower bounds in the Z direction. The model contained 333,030 atom. To investigate the interaction between the solute atom and the misfit dislocation on the interface, the W atom was placed far away from the intersection of the two dislocations. Ni or Al atoms in different (0 0 1) planes near the γ/γ' interface were substituted by the W atom. The misfit dislocations were formed after the systems were fully relaxed at 0 K with a time step of 5×10^{-15} s using the present EAM potential. The atomic structures of the dislocations are visualized by the Common Neighbor Analysis [95] (CNA), which is presented in Fig. 8. There are two types of stacking sequence, the atom structures are constructed and plotted in the inset sketches of Fig. 9. The atom structure plotted in the inset sketch of Fig. 9(a) is identical with that of Fig. 9(c), and the atom structure plotted in the inset sketch of Fig. 9(b) is identical with that of Fig. 9(d). The expression $E_I(R_d, n) = E(R_d, n) - E(\infty, n)$ describes the W-dislocation interaction energy. R_d is the distance between the W atom and the dislocation core center, $E(R_d, n)$ and $E(\infty, n)$ are the total energies of the system with the W located at R_d and the total$n$th (0 0 1) plane, respectively. The same method [28] was carried out to study the pinning effect of Co.

E_I of two types of stacking sequence as a function of the distance from the dislocation core to the solute atom (W or Co) along the [1 1 0] direction is plotted in Fig. 9. It can be found from Fig. 9(a) and (b) that the absolute value of interaction energy E_I decreases with the increasing of the distance from the dislocation core to the W impurity when W substituted at different sites in the same (0 0 1) plane, which means that the interaction becomes weaker as the distance increases.
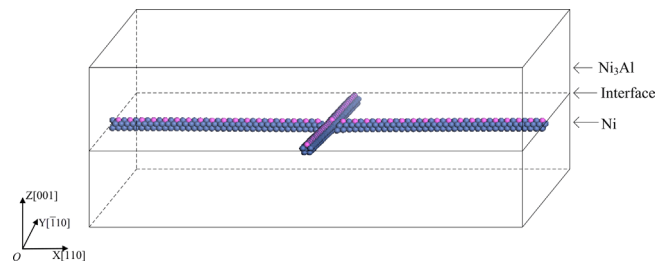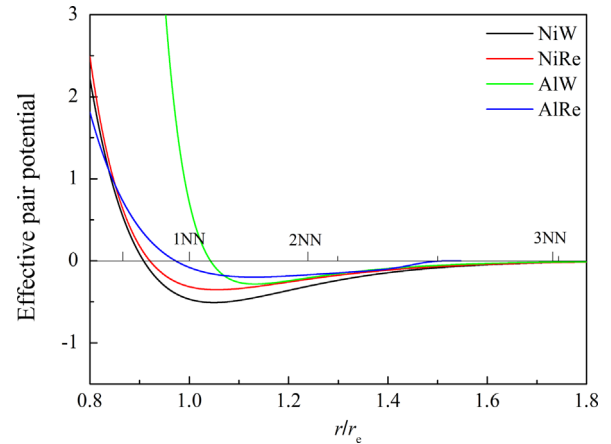

Fig. 8. The relaxed lattice misfit dislocation on the γ(Ni)/γ'(Ni$_3$Al) interface visualized by the Common Neighbor Analysis. The blue and red balls denote Ni and Al atoms, respectively.
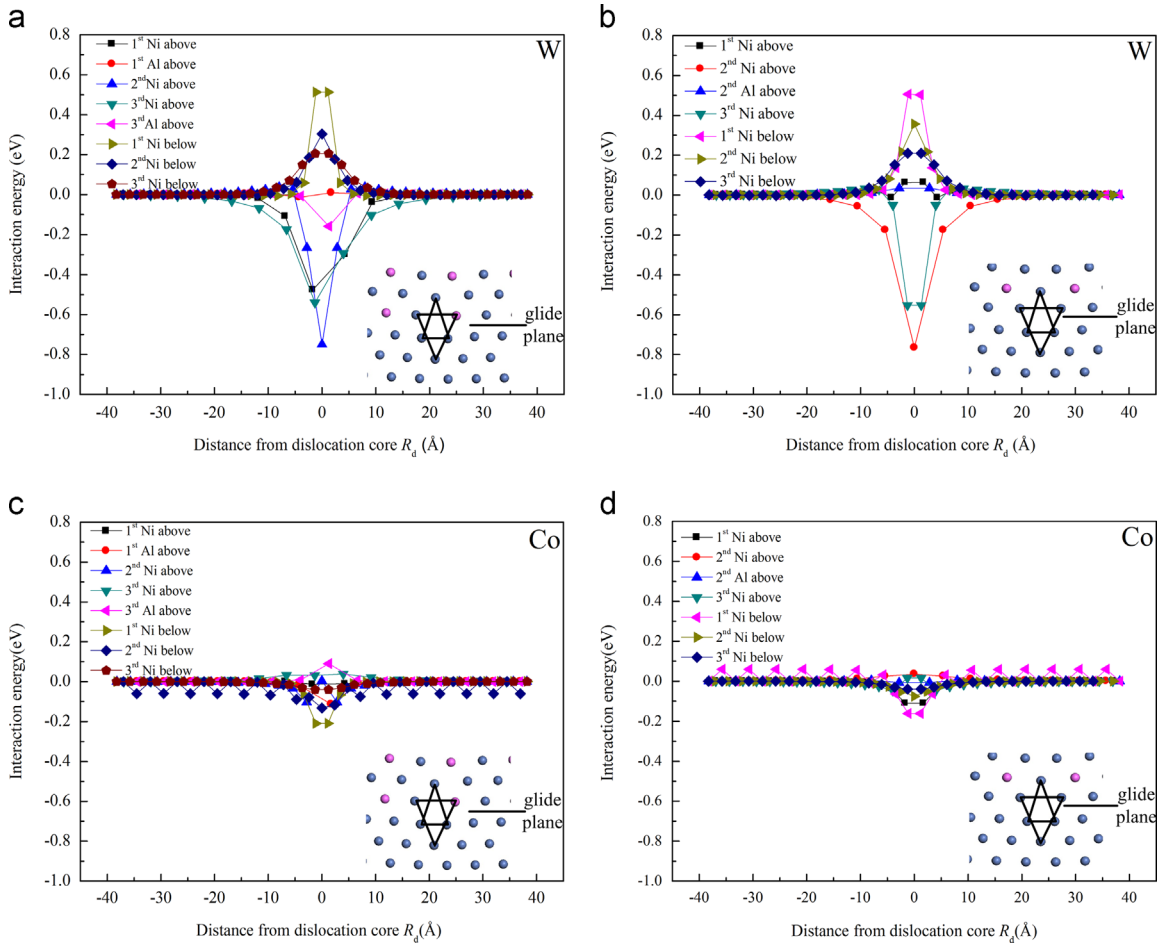
Fig. 9. The interaction energy between solute atom (W, Co) and the misfit dislocation of two stacking sequence types (a), (c) and (b), (d). The blue and red balls denote Ni and Al atoms, respectively.

The interaction is negative (or positive) when the solute atom is above (or under) the glide plane except when the W impurity is located in the dislocation core at the first (0 0 1) plane. This reveals that the misfit dislocation can attract the W impurity that is located in γ'(Ni₃Al) but repel the W impurity that is located in γ(Ni). The simulation result can be explained as follows. The γ'(Ni₃Al) is in expansive state and the γ(Ni) is under compressive stress in the vicinity of the misfit dislocation. W induces a lattice expansion because of its bigger atomic radius. The lattice becomes less deformed when the atom in the γ'(Ni₃Al) region is substituted by W atom. In this case, the interaction energy is negative and the dislocation attracts the solute. Thus the system is more stable. On the contrary, the lattice becomes more highly compressed when W located in the γ(Ni) region. In this case, the interaction energy is positive and the dislocation repels the solute. The most negative interaction energies in two stacking sequence types (a) and (b) are -0.75 eV and -0.77 eV, respectively, when the Ni atom in the second (0 0 1) plane above the glide plane is substituted by W. It can be found from Fig. 9(c) and (d) that the absolute value of interaction energies E_I between Co and the misfit dislocation are much smaller. The most negative interaction energies in the two stacking sequence types (c) and (d) are -0.21 eV and -0.16, respectively, when the Ni atom in the first (0 0 1) plane below the glide plane is substituted by Co. The pining effect of Co on the misfit dislocation is much weaker and negligible because of its smaller atomic radius (similar with Ni) [96].

Compared with the Re-dislocation interaction energies of -0.53 eV for type(a) and -0.60 eV for type (b) [28], the W-dislocation interaction energies are more negative, which means the pinning effect of W is stronger than that of Re. The

effective potential of Ni–W, Ni–Re, Al–W and Al–Re are plotted in Fig. 10, and r_e is the equilibrium atomic distance of L1₂–Ni₃Al with perfect crystal structure. The distances of Ni–X and Al–X (X=W, Re) are larger than r_e since the γ'(Ni₃Al) is in expansive state. It can be seen from Fig. 10 that the binding energy of Ni–W is more negative than that of Ni–Re between the first- and third-neighbor distances. However, no such feature is found between Al–W and Al–Re interaction. Hence the more negative binding energy of Ni–W is the main cause of the stronger pinning effect of W on the misfit dislocation than Re. We also correlate the pinning effect of

Fig. 10. The effective pair potentials of Ni–W, Ni–Re, Al–W and Al–Re, and r_e is the equilibrium atomic distance of L1₂–Ni₃Al.

alloying element with the atomic radius. As for Co, Re and W, the pinning effect increases with the increasing of the atomic radius (Co < Re < W). Nevertheless, further study is needed to verify the interrelation between the pining effect and the atomic radius.

4. Conclusions

A ternary Ni–Al–W embedded-atom-method (EAM) potential has been constructed for the γ(Ni)/γ'(Ni$_3$Al) superalloys based on experiments and first-principles calculations. Both the site preference of W in the γ'(Ni$_3$Al) phase and the interaction between W and the γ(Ni)/γ'(Ni$_3$Al) interface are considered in the construction of the potential. The potential predicts that the W atoms do not tend to form clusters in γ(Ni), which is consistent with experiments. Using the present potential, the impurity diffusion coefficient of W in γ(Ni) using the five-frequency model is calculated. The obtained effective diffusion activation energy Q_e and the pre-exponential factor D_0 determined by fitting the diffusion coefficients are in reasonable agreement with experimental results. The effects of W on the interface lattice misfit between γ(Ni) and γ' (Ni$_3$Al) as well as the elastic constants of γ'(Ni$_3$Al) are also in good agreement with the first-principles calculation results. By the addition of W, the lattice misfit decreases and the elastic constants of γ'(Ni$_3$Al) increase. The pinning effect of W on the γ(Ni)/γ'(Ni$_3$Al) interface misfit dislocation is stronger than that of Re. This can be attributed to the more negative binding energy of Ni–W. As for alloyed elements Co, Re and W, the pinning effect increases with the increasing of the atomic radius.

References

[1] R.C. Reed, The Superalloys: Fundamentals and Applications, Cambridge University Press, Cambridge, 2006.
[2] C.T. Sims, N.S. Stoloff, W.C. Hagel (Eds.), Superalloys II—High Temperature Materials for Aerospace and Industrial Applications, Wiley, New York, 1987.
[3] R.C. Reed, T. Tao, N. Warnken, Acta Mater. 57 (2009) 5898–5913.
[4] C.L. Zacherl, S.L. Shang, D.E. Kim, Y. Wang, Z.K. Liu, Superalloys 2012 (2012) 455–461.
[5] I.M. Razumovskii, A.V. Ruban, V.I. Razumovskiy, A.V. Logunov, V.N. Larionov, O. G. Ospennikova, V.A. Poklad, B. Johansson, Mater. Sci. Eng., A 497 (2008) 18–24.
[6] C.K. Sudbrack, D. Isheim, R.D. Noebe, N.S. Jacobson, D.N. Seidman, Microsc. Microanal. 10 (2004) 355–365.
[7] S. Wöllmer, T. Mack, U. Glatzel, Mater. Sci. Eng., A 319 (2001) 792–795.
[8] T. Yokokawa, M. Osawa, K. Nishida, T. Kobayashi, Y. Koizumi, H. Harada, Scr. Mater. 49 (2003) 1041–1046.
[9] C.K. Sudbrack, T.D. Ziebell, R.D. Noebe, D.N. Seidman, Acta Mater. 56 (2008) 448–463.
[10] A. Volek, F. Pyczak, R.F. Singer, H. Mughrabi, Scr. Mater. 52 (2005) 141–145.
[11] Y. Amouyal, Z.G. Mao, C. Booth-Morrison, D.N. Seidman, Appl. Phys. Lett. 94 (2009) 041917–041919.
[12] Y. Amouyal, Z.G. Mao, D.N. Seidman, Appl. Phys. Lett. 93 (2008) 201905–201907.
[13] K. Chen, L.R. Zhao, J.S. Tse, Mater. Sci. Eng., A 365 (2004) 80–84.
[14] J.S. Duan, J. Phys: Condens. Matter. 18 (2006) 1381–1384.
[15] J.S. Duan, J. Phys: Condens. Matter 19 (2007) 086217–086225.
[16] T. Zhu, C.Y. Wang, Phys. Rev. Br 72 (2005) 014111–014116.
[17] C. Kohler, P. Kizler, S. Schmauder, Mater. Sci. Eng. A 400-401 (2005) 481–484.
[18] H.X. Xie, C.Y. Wang, T. Yu, Modell. Simul. Mater. Sci. Eng. 17 (2009) 055007–055016.
[19] W.P. Wu, Y.F. Guo, Y.S. Wang, R. Mueller, D. Gross, Philos. Mag. 91 (2011) 357–372.
[20] B. Hess, B.J. Thijsse, E. Van der Giessen, Phys. Rev. B 71 (2005) 054111–054120.
[21] H.X. Xie, C.Y. Wang, T. Yu, J. Mater. Res. 23 (2008) 1597–1603.
[22] Z.G. Liu, C.Y. Wang, T. Yu, Modell. Simul. Mater. Sci. Eng. 21 (2013) 045009–045022.
[23] S.M. Foiles, M.S. Daw, J. Mater. Res. 2 (1987) 5–15.
[24] A.F. Voter, S.P. Chen, Mater. Res. Soc. Symp. Proc. 82 (1987) 175–181.
[25] Y. Mishin, Acta Mater. 52 (2004) 1451–1467.
[26] G.P. Purja Pun, Y. Mishin, Philos. Mag. 89 (2009) 3245–3267.
[27] X.Y. Yang, W.Y. Hu, J. Appl. Phys. 115 (2014) 153507–153515.
[28] J.P. Du, C.Y. Wang, T. Yu, Modell. Simul. Mater. Sci. Eng. 21 (2013) 015007–015033.
[29] J.P. Du, C.Y. Wang, T. Yu, Chin. Phys. B 23 (3) (2014) 033401–033408.
[30] J. Cai, Y.Y. Ye, Phys. Rev. B 54 (1996) 8398–8410.
[31] M.S. Daw, M.I. Baskes, Phys. Rev. Lett. 50 (1983) 1285–1288.
[32] M.S. Daw, M.I. Baskes, Phys. Rev. B 29 (1984) 6443–6453.
[33] A. Banerjea, J.R. Smith, Phys. Rev. B 37 (1988) 6632–6645.
[34] B. Delley, J. Chem. Phys. 92 (1990) 508–517.
[35] B. Delley, J. Chem. Phys. 113 (2000) 7756–7764.
[36] Y. Mishin, M.J. Mehl, Phys. Rev. B 65 (2002) 224114–224127.
[37] J.H. Rose, J.R. Smith, F. Guinea, J. Ferrante, Phys. Rev. B 29 (1984) 2963–2969.
[38] R.A. Johnson, D.J. Oh, J. Mater. Res. 4 (1989) 1195–1201.
[39] M.W. Finns, J.E. Sinclair, Philos. Mag. A 50 (1984) 45–55.
[40] B. Lee, M.I. Baskes, H. Kim, Y.K. Cho, Phys. Rev. B 64 (2001) 184102–184112.
[41] W.Y. Hu, X.L. Shu, B.W. Zhang, Comput. Mater. Sci. 23 (2002) 175–189.
[42] C. Kittel, Introduction to Solid State Physics, seventh ed., John Wiley and Sons Inc, New York, Chichester, Brisbane, Toronto, Singapore, 1996.
[43] W. Martienssen, H. Warlimont, Springer Handbook of Condensed Matter and Materials, Springer, Berlin, Heidelberg, New York, 2006.
[44] K. Maier, M. Peo, B. Saile, H.-E. Schaefer, A. Seeger, Philos. Mag. A 40 (1979) 701–728.
[45] P. Ehrhart, Atomic Defects in Metals, vol. 25, Springer, Berlin, 1991.
[46] A.M. Guellil, J.B. Adams, J. Mater. Res. 7 (1992) 639–652.
[47] J.M. Harder, D.J. Bacon, Philos. Mag. A 54 (1986) 651–661.
[48] W.R. Tyson, W.A. Miller, Surf. Sci. 62 (1977) 267–276.
[49] F.R. de Boer, R. Boom, W.C.M. Mattens, A.R. Miedema, A.K. Niessen, Cohesion in Metals, Amsterdam, North-Holland, 1988.
[50] S.L. Frederiksen, K.W. Jacobsen, Philos. Mag. 83 (2003) 365–375.
[51] H.E. Grenga, R. Kumar, Surf. Sci. 61 (1976) 283–290.
[52] G. Kresse, J. Hafner, Phys. Rev. B 48 (1993) 13115–13118.
[53] G. Kresse, J. Furthmuller, Phys. Rev. B 54 (1996) 11169–11186.
[54] C. Jiang, B. Gleeson, Scr. Mater. 55 (2006) 433–436.
[55] D. Blavette, E. Cadel, C. Pareige, B. Deconihout, P. Caron, Microsc. Microanal. 13 (2007) 464–483.
[56] P. Peng, A.K. Soh, R. Yang, Z.Q. Hu, Comput. Mater. Sci. 38 (2006) 354–361.
[57] A. Mottura, M.K. Miller, R.C. Reed, Superalloys 2008, The Minerals, Metals&Materials Society, Warrendale, PA (2008) 891–900.
[58] A. Mottura, R.T. Wu, M.W. Finnis, R.C. Reed, Acta Mater. 56 (2008) 2669–2675.
[59] A. Mottura, N. Warnken, M.K. Miller, M.W. Finnis, R.C. Reed, Acta Mater. 58 (2010) 931–942.
[60] A. Janotti, M. Krčmar, C.L. Fu, R.C. Reed, Phys. Rev. Lett. 92 (2004) 085901–085904.
[61] M. Krčmar, C.L. Fu, A. Janotti, R.C. Reed, Acta Mater. 53 (2005) 2369–2376.
[62] T.M. Pollock, A.S. Argon, Acta Metall. Mater. 40 (1992) 1–30.
[63] N. Matan, D.C. Cox, C.M.F. Rae, R.C. Reed, Acta Mater. 47 (1999) 2031–2045.
[64] A. Sato, Y.L. Chiu, R.C. Reed, Acta Mater. 59 (2011) 225–240.
[65] Q. Wu, S.S. Li, Y. Ma, S.K. Gong, Chin. Phys. B 21 (2012) 109102–109108.
[66] A.D. LeClaire, A.B. Lidiard, Philos. Mag. 1 (1956) 518–527.
[67] A.D. LeClaire, J. Nucl. Mater. 69/70 (1978) 70–96.
[68] M. Mantina, Y. Wang, L.Q. Chen, Z.K. Liu, C. Wolverton, Acta Mater. 57 (2009) 4102–4108.
[69] J.B. Adams, S.M. Foiles, W.G. Wolfer, J. Mater. Res. 4 (1989) 102–112.
[70] G. Neumann, V. Tolle, Philos. Mag. A V54 (5) (1986) 619–629.
[71] R.A. Swalin, A. Martin, Trans. AIME 206 (1956) 567–572.
[72] K. Monma, H. Suto, H. Oikawa, J. Jpn. Inst. Met. 28 (1964) 197–200.
[73] M.S.A. Karunaratne, P. Carter, R.C. Reed, Mater. Sci. Eng., A 281 (2000) 229–233.
[74] C.E. Campbell, W.J. Boettinger, U.R. Kattner, Acta Mater. 50 (2002) 775–792.
[75] M.S.A. Karunaratne, D.C. Cox, P. Carter, R.C. Reed, Superalloys 2000, The Minerals, Metals&Materials Society, Warrendale, PA (2000) 263–272.
[76] S. Neumeier, F. Pyczak, M. Göken, Superalloys 2008, The Minerals, Metals&Materials Society, Warrendale, PA (2008) 109–119.
[77] L.J. Carroll, Q. Feng, J.F. Mansfield, T.M. Pollock, Mater. Sci. Eng., A 457 (2007) 292–299.
[78] U. Glatzel, M. Feller-Kniepmeier, Scr. Metall. 23 (11) (1989) 1839–1844.
[79] J.F. Ganghoffer, A. Hazotte, S. Denis, A. Simon, Scr. Metall. 25 (1991) 2491–2496.
[80] Y.J. Wang, C.Y. Wang, Mater. Res. Soc. Symp. Proc. 1224 (2009) FF05-31.
[81] F.A. Mauer, R.G. Munro, G.J. Piermarini, S. Block, D.P. Dandekar, J. Appl. Phys. 58 (1985) 3727–3730.
[82] P. Wallow, G. Neite, W. Schröer, E. Nembach, Phys. Status Solidi A 99 (1987) 483–490.
[83] F.X. Kayser, C. Stassis, Phys. Status Solidi A 64 (1981) 335–342.
[84] K. Ono, R. Stern, Trans. Metal. Soc. AIME 245 (1969) 171–172.
[85] J.X. Zhang, T. Murakumo, Y. Koizumi, T. Kobayashi, H. Harada, S. Masaki, JR., Metall. Mater. Trans. A 33 (2002) 3741–3746.
[86] J.X. Zhang, T. Murakumo, Y. Koizumi, T. Kobayashi, H. Harada, J. Mater. Sci. 38 (2003) 4883–4888.
[87] J.X. Zhang, T. Murakumo, Y. Koizumi, T. Kobayashi, H. Harada, Acta Mater. 51 (2003) 5073–5081.

[88] S.G. Tian, H.H. Zhou, J.H. Zhang, H.C. Yang, Y.B. Xu, Z.Q. Hu, Mater. Sci. Eng., A 279 (2000) 160–165.
[89] N. Clément, M. Benyoucef, M. Legros, P. Caron, A. Coujou, Mater. Sci. Forum 509 (2006) 57–62.
[90] J.Y. Buffiere, M. Ignat, Acta Metall. Mater. 43 (5) (1995) 1791–1797.
[91] D. Blavette, L. Letellier, A. Racine, A. Hazotte, Microsc. Microanal. Microstruct. 7 (3) (1996) 185–193.
[92] J.Y. Buffiere, M.C. Chcynct, M. Ignat, Scr. Mater. 34 (3) (1996) 349–356.
[93] C. Carry, J.L. Strudel, Acta Metall. 25 (1977) 767–777.
[94] D.F. Lahrman, R.D. Field, R. Darolia, H.L. Fraser, Acta Metall. 36 (1988) 1309–1320.
[95] D. Faken, H. Jónsson, Comput. Mater. Sci. 2 (1994) 279–286.
[96] P. Linus, J. Am. Chem. Soc. 69 (3) (1947) 542–553.